In Situ Spectroscopic Study of the Optomechanical Properties of Evaporating Field Ion Emitters

P. Dalapati, G. Beainy, Enrico Di Russo, Ivan Blum, Jonathan Houard, Simona Moldovan, Angela Vella, François Vurpillot, N. Le Biavan, M. Hugues, et al.

Published as Physical Review Applied, 15, 024014 (2021)

DOI: 10.1103/PhysRevApplied.15.024014

In-situ spectroscopic study of the opto-mechanical properties of evaporating field ion emitters

P. Dalapati[1†], G. Beainy[1], E. Di Russo[1], I. Blum[1], J. Houard[1], S. Moldovan[1], A. Vella[1], F. Vurpillot[1], N. Le Biavan[2], M. Hugues[2], J.M. Chauveau[2], L. Rigutti[1].

1) UNIROUEN, CNRS, Groupe de Physique des Matériaux, Normandie Université, 76000 Rouen, France.
2) Université Cote d'Azur, CNRS, CRHEA, 06 905 Sophia Antipolis CEDEX, France

[†]Current affiliation: Research Center for Nano-Devices and Advanced Materials, Nagoya Institute of Technology, Nagoya 466-8555, Japan

*Correspondence to: lorenzo.rigutti@univ-rouen.fr

ABSTRACT - The possibility of measuring *in-situ, operando* photoluminescence spectroscopy within a photonic atom probe allows for real time study of the mechanical stress state within a field emitter either statically, as a function of the field-induced tensile stress or dynamically, as a result of the evolution of the shape of the emitter upon its evaporation. The dynamic evolution results from the relaxation of the strain induced by lattice mismatch and by the propagation of the stress from the apex while the morphology of the field emitter changes. The opto-mechanical information can be interpreted through the three-dimensional atomic scale images of the chemical composition of the emitter obtained through standard atom probe analysis. In the present work, the photoluminescence signal of a ZnO/(Mg,Zn)O quantum well allows for the local measurement of strain within the well and of the electrostatic field applied to the apex of the nanoscale field emitter.

I. INTRODUCTION

The measurement of strain states in nanoscale systems is nowadays possible by means of different techniques. Remarkable situations include the measurement of strain in transmission electron microscopes (TEM) by geometric phase analysis [1] or holographic interferometry [2] in field effect transistors, heterostructures, nanowires. The access to strain state can also be obtained by cross-sectional scanning tunneling microscopy (X-STM), generally by measurement of the relief of the scanned surface due to out-of-plane lattice relaxation in semiconductor superlattice or quantum dot structures [3,4], as well as in metallic structures [5]. Alternatively, 3D strain/stress maps can be obtained by x-ray nanoprobes from synchrotron light [6,7].

Strain may have important effects on the optical and electrical properties of nanoscale systems. Strain engineering may be appropriate to the manipulation of energy bands, and can influence the optical signature of emitting or absorbing centers [8,9] and the electrical transport in semiconducting channels [10]. It may be applied either by a proper design of the nanoscale system, for instance exploiting lattice mismatch in heterostructures [9] or by an external action producing in a controlled way hydrostatic [11,12] or uniaxial stress [13,14].

In this contribution, we report about an original way to access to the stress state of nanoscale field ion emitters through the use of a photonic atom probe (PAP) [15,16], whose principles are schematically illustrated in fig. 1. This instrument consists in a laser-assisted tomographic atom probe, in which a needle-shaped nanoscale specimen (field ion emitter) is progressively submitted to the evaporation of constituent ions under the combined action of a static DC field and of laser pluses which trigger the process. As in any tomographic atom probe, ion evaporation provides a 3D image of the chemical composition of the specimen. The particular

feature of the PAP instrument is that light collection optics is applied to the in-situ analysis of the photoluminescence (PL) produced by the field emitter under the same laser excitation used for ion evaporation. As a result, it is possible to obtain a 3D image of quantum emitters coupled with their optical signature. However, beyond the interest of this instrument in the framework of nanoscale microscopy, we demonstrate in this work that PAP allows for the in-situ, operando measurement of the strain state of a field emitter, which is due both to the strain relaxation due to the evaporation of heterostructure layers with different lattice constants and to the application of the DC field responsible for the specimen evaporation.

This work is structured as follows. Section II describes the experimental techniques and methods. Then, the PAP analysis of ZnO/(Mg,Zn)O quantum well heterostructures is presented in section III. In section IV the theory of stress and strain in non-evaporating and evaporating field emitters is developed. Finally, the connection between the theory and the experiment is drawn in the discussion of section V.

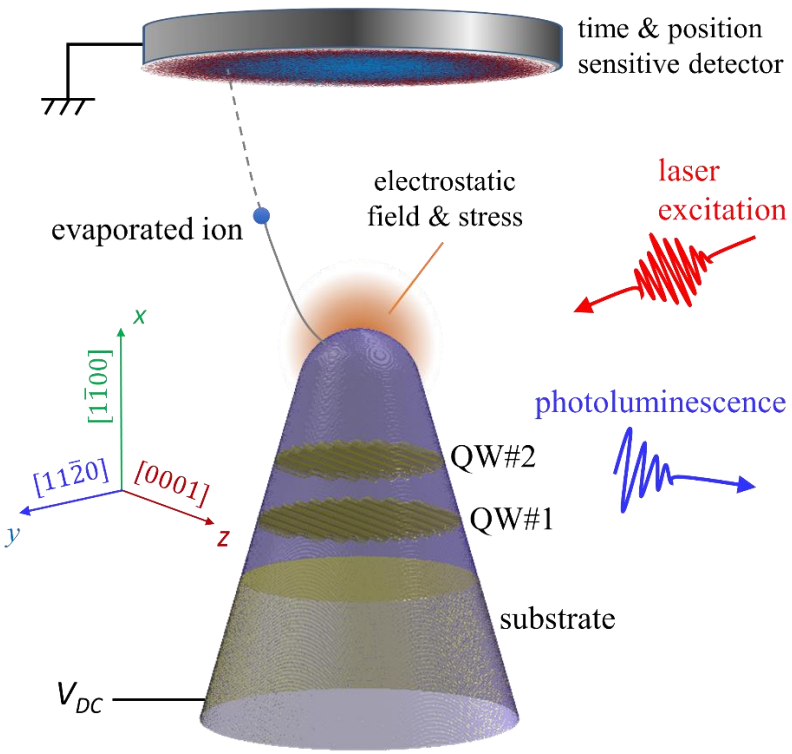

Fig. 1 Schematic representation of the experimental setup and of the analyzed system. The orientation of the crystal constituting the field emitter is also reported.

II. EXPERIMENTAL

- ***Sample growth and properties***

Plasma assisted molecular beam epitaxy (PA-MBE) was used to grow the ZnO/(Zn,Mg)O homoepitaxial MQWs on an *m*-plane (1-100) wurtzite (WZ) ZnO substrate. Details on the homoepitaxial growth can be found in Ref. [17]. The structures contain two ZnO QWs and (Mg,Zn)O barriers. The total thickness and the alloy composition of the multi-layer structure were designed in order to avoid plastic relaxation.

- ***Tip specimen preparation***

Needle shaped field emitters were prepared by Focused Ion Beam (FIB) in a ZEISS Nvision40 dual beam SEM-FIB system. The preparation consisted in the standard protocol of lift-out and milling using and acceleration voltage of 30 kV for the Ga ions during sample milling, with a final cleaning step at 2 kV [18]. This protocol is designed to preserve a PL signal from the QW#1 and from the (Mg,Zn)O barrier detectable in the PAP system, while the signal of QW#2 (closer to the tip apex) is generally quenched by the damage introduced by the Ga ions. With ions at 30 keV, FIB is expected to produce surface amorphization over several nm at grazing incidence, and introduction of non-radiative recombination centers over several tens of nm [19]. In the present structures, FIB induces irreversible damage to the optical properties the whole

region of interest of around 50 % of the fabricated tips. In the latter case, only the signal of the ZnO substrate is detectable. Several tip specimens were analyzed in this work, yielding consistent results. Notice that alternative preparation methods could be considered in order to increase the success rate of preparation of specimens from thin films, such as using plasma-FIB [20], which is known to introduce less impurities, or directly synthesize quantum emitter structures within nanowires [21]. The tip specimen for which the detailed analysis is reported in the main text of this contribution is visible in the scanning electron micrograph presented in Fig. 2-(a).

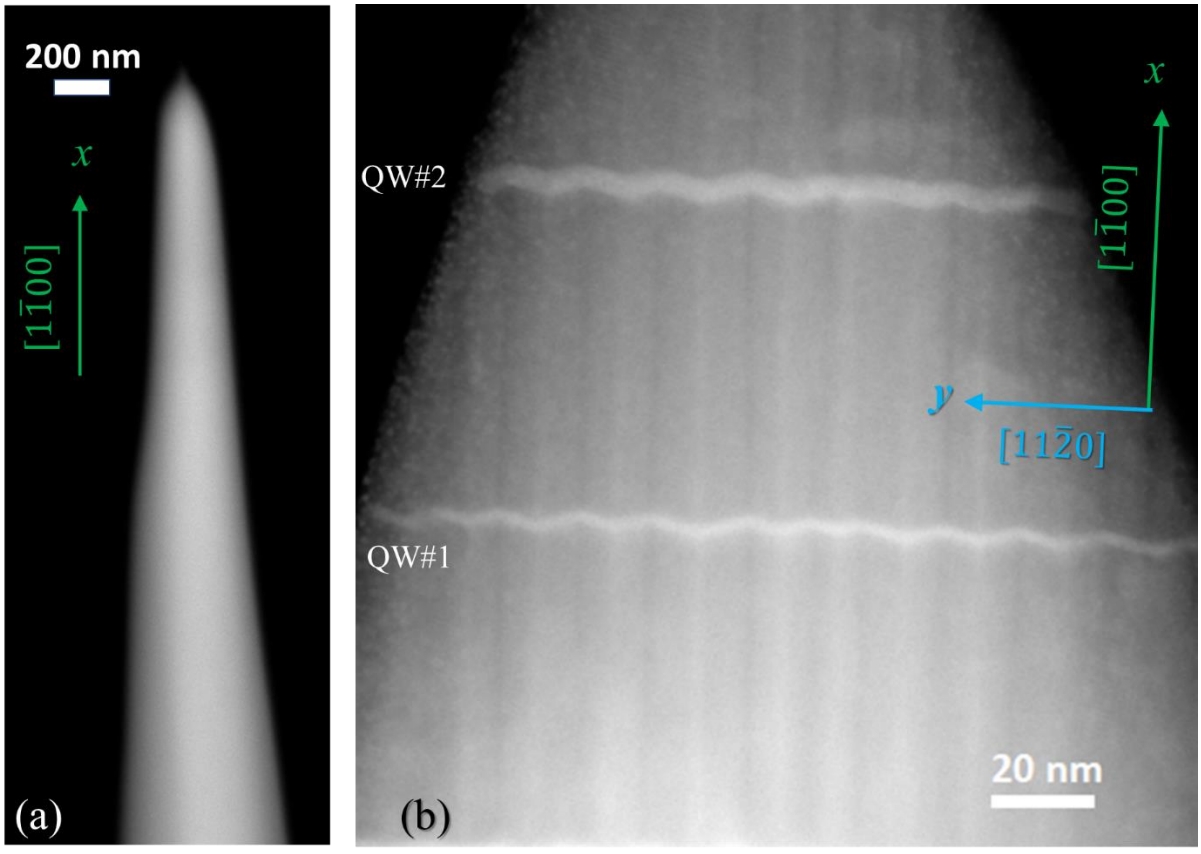

Fig. 2 (a) Scanning electron micrograph of the analyzed tip, (b) transmission electron micrograph and crystal orientation of a field emitter extracted from the ZnO/(Mg,Zn)O heterostructure system.

- ***Tip specimen preliminary characterization and crystal orientation***

Transmission Electron Microscopy (TEM) assays were carried out on prepared tip specimens with a double corrected analytical Jeol JEM-ARM200CF, operated at 200kV. During the Scanning TEM (STEM) experiments, a 0.9 Å probe scans the specimen surface and two simultaneous micrographs were registered under a Bright Filed circular detector (BF-STEM) and a High Angle Annular Dark Field (HAADF) detector. In HAADF detection, the image intensity approximately scales with the square of the Z atomic number of the material under examination. the high intensity areas correspond to regions rich in Zn, allowing one to determine the thickness of the QWs by direct measurements. The thicknesses of the QWs measured by STEM-HAADF are t_1 = (2.0±0.1) nm and t_2 = (3.9±0.1), respectively. Notice that, as STEM performed at 200 keV may introduce non-radiative recombination centers, the tip specimen reported in Fig. 2-(b) is not one of those analyzed by PAP. The sawtooth profile of the QWs clearly marks the morphology of these QWs. This profile is actually that of the ZnO substrate surface before the epitaxial growth of the multi-QW/barrier system, and it propagates throughout the epitaxial growth of the latter [22]. This profile is susceptible to induce compositional inhomogeneities within the barriers, with the formation of Zn- and Mg- enriched regions corresponding to the edges pointing towards the substrate and towards the upper surface, respectively. The results reported in Fig. 2-(b) and later on in the section dedicated to the PAP study show that the barriers exhibit a decomposition behavior similar to that reported in the detailed study of Ref. [22]. These compositional inhomogeneities are related to the sawtooth morphology. No evidence for the presence or introduction of dislocations or other extended defects was found.

All prepared tips have the axis oriented along the [1-100] direction (*m*-direction) of the wurtzite crystal, which also corresponds to the *x* axis of the reference system in which the stress/strain tensors are defined. The sawtooth profile is visible when the observation is performed along the

polar [0001] direction (*c*-direction, *z* axis for the strain/stress tensors) [22]. The [11-20] *a*-direction corresponds to the *y* axis for the strain/stress tensors. The orientation of the crystal is also visualized in Fig. 1 and the correspondences between the tip reference frame and the crystal directions is specified in Table 1.

Table 1. Correspondences between the tip frame and the crystal directions

Directions in the tip reference frame		**Crystal directions**	
Tip axis	x	$[1\bar{1}00]$	m
	y	$[11\bar{2}0]$	a
	z	[0001]	c

- ***Photonic Atom Probe setup***

As mentioned in the introduction, the schematics of the PAP is reported in Fig. 1, while the technical details of the instrument used in this study are discussed in Ref. [15]. The nanometric needle-shaped specimen is polarized with a voltage V_{DC} = 3 - 16 kV, leading to an apex electric field of a few tens of V/nm [23,24]. Field ion evaporation is then triggered by femtosecond laser pulses at the repetition rate of 400 kHz. The specimen apex is illuminated by a laser spot with size close to one micron and an average power of 10 µW. The spot size is limited by the imperfections of optical elements and is larger than the diffraction limit $w \approx \lambda/(2NA) = 443$ nm, where $\lambda = 266$ nm is the laser wavelength and NA = 0.3 is the numerical aperture of the focusing optics. PL spectra were acquired with a 600/mm grating in a 320 mm focal length spectrometer, with a spectral resolution of around 0.3 nm. The CCD array integration time for each acquisition was set to 90 s.

The evaporated ions are detected by a time resolved and position sensitive detector [25], which provides the impact position of ions and their time of flight. The first information is used to calculate the position of evaporated atoms at the tip surface, while the second is used to compute mass/charge ratios that enable to identify the chemical nature of ions, as shown in the mass spectrum of Fig. 3-(a). The in-depth layer by layer evaporation of the specimen makes the 3D reconstruction of atomic positions possible. 3D maps of the chemical composition of the specimen can thus be derived. The instrument is able to collect and analyze *in-situ* and *operando* the photoluminescence that laser pulses excite simultaneously with surface atom evaporation.

The collection of the PL signal during atom probe tomography (APT) translates into a series of spectra which are indexed by the integer i_{PL} while keeping track of the progressive number of detected atoms. This has recently been shown to enable super-resolution optical spectroscopy, as spectral signatures of closely-lying emitters can be discriminated. This possibility is not exploited in this work, in which a single emitter is studied [16]. PL has also been collected during a slow initial voltage ramp, with steps at a set of bias values, in order to obtain complementary information on the field-induced strain [26,27].

III. PHOTONIC ATOM PROBE EXPERIMENT

In the following the PAP experiment is described. After the initial voltage ramp, evaporation took place at a detection rate set in the interval Φ = 0.003-0.004 ions/pulse. The specimen base temperature was set at 30 K.

- ***Mass spectrum***

The mass spectrum is shown in Fig. 3-(a), and contains the atomic and molecular ionic species usually found in the analysis of (Mg,Zn)O [22,28]. The interpretation of the mass spectra should consider the superimposition of peaks associated to different atomic and molecular species: the peak at 32 Da corresponds to an overlap of $^{64}Zn^{2+}$ and O_2^+ [22]. Considering the natural abundance of Zn isotopes in the mass range 31-37 Da it is possible to calculate the respective total amount of zinc and oxygen; the same method has been adopted in the mass range 78-89 Da where the existing peaks are attributed to both ZnO^+ and $Zn_2O_2^{2+}$. The analysis of the Zn^{2+}/Zn^+ charge state ratio is a useful indicator of the intensity of the microscopic field (i.e. the field responsible for ion evaporation, usually higher than the average field) [29]. This ratio is approximately equal to 0.5 through the barrier, which indicates that the field may be assumed as constant; Furthermore, this ratio corresponds to a microscopic field F_μ ~20 V/nm, which is favorable to composition measurements in (Mg,Zn)O [28]. Separate APT analysis were performed with another instrument (a Laser-assisted Wide-angle Tomographic Atom Probe, used in recent works on composition metrology [30,28]) in order to confirm the measurement of composition within the barriers.

- ***Voltage curve***

The voltage applied to the tip is reported in Fig. 3-(b) versus the index i_{PL} of the PL spectra acquired during tip evaporation. The same plot also contains the relationship between PL spectral index and the number of detected atoms. Evaporation takes place between $V_{e,s}$ = 6 kV

(starting evaporation voltage) and $V_{e,f}$ = 10.3 kV (final evaporation voltage). The ratio between these two values is fairly consistent with the ratio of the initial and final radii that can be visually assessed by the analysis of the SEM image of the tip (Fig-2-(a)), i.e. R_i = (48±5) nm, R_f = (88±5) nm. The continuous increase in the radius of the tip during evaporation forces a rise of the voltage in order to maintain a constant detection rate. Remarkably, the curve is non-monotonous: two dips are clearly visible after i_{PL} = 60 and after i_{PL} = 95. These local minima correspond to the evaporation of the two ZnO QWs which have a lower cohesive energy than their surrounded (Mg,Zn)O barriers, and consequently, the surface field needed for its evaporation at constant detection rate is lower. The local decrease of the applied voltage translates into the decrease of the apex field intensity. The experiment was concluded when the evaporation reached the ZnO substrate.

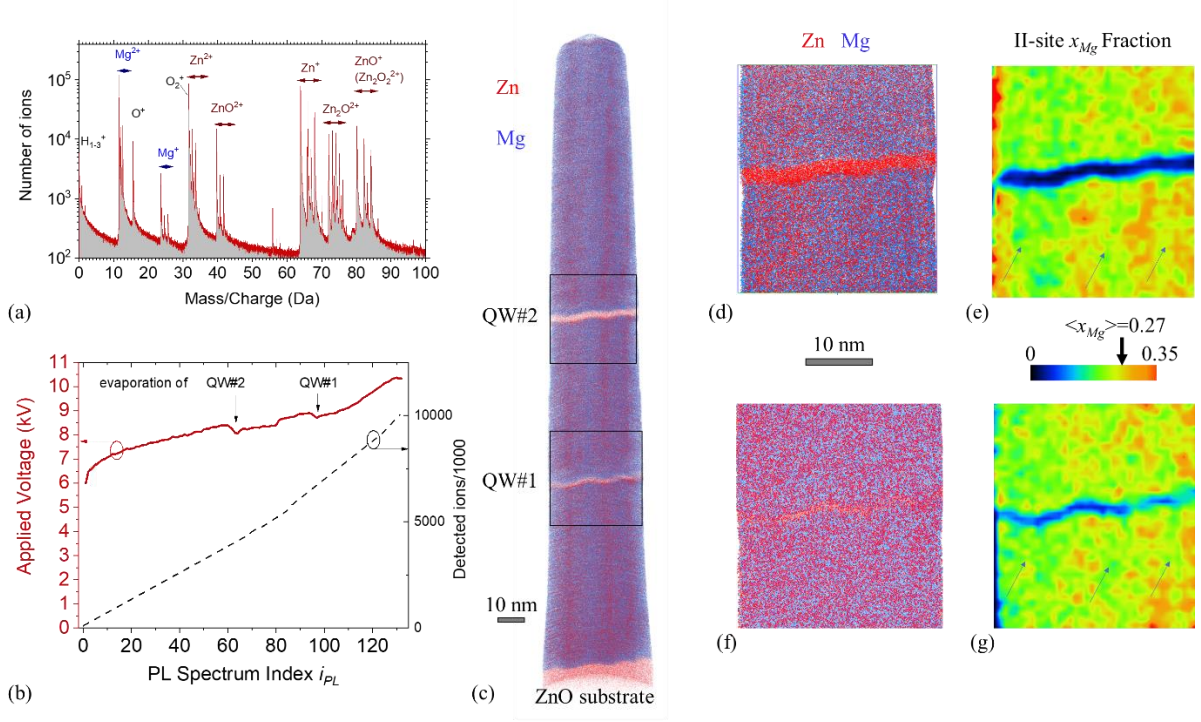

Fig. 3. Atom Probe Tomography analysis. (a) Mass spectrum indicating the main ionic species, (b) Voltage curve and progressive number of detected atoms as a function of the index of the PL spectrum i_{PL}; (c) Three-dimensionally reconstructed volume of the analyzed field emitter. 100% of the Mg ions are reported in blue, 30% of the Zn+ and Zn2+ ions are reported in red (both classes of detection events are traced with a 0.2 level of

transparency). (d) Close-up of the distribution of Zn and Mg ions in a 5 nm thick slice intersecting the axis of the tip at the depth of QW#2, (e) II-site fraction map of the slice reported in (d). (f) Close-up of the distribution of Zn and Mg ions in a 5 nm thick slice intersecting the axis of the tip at the depth of QW#1, (g) compositional map of the slice reported in (f). The arrow above the color scale indicates the average value of the Mg II-site fraction $\langle x_{Mg} \rangle = 0.27$ of the (Mg,Zn)O barrier.

- ***3D reconstruction***

The 3D reconstructed volume of the analyzed system is visualized in Fig. 3-(c), and it was obtained by the application of a reconstruction algorithm based on the evolution of the applied voltage [31]. The following set of parameters was used: Apex Field = 16.8 V/nm, Projection point m+1 = 1.65, Curvature factor = 1.5 and reconstruction detection efficiency $\eta_{rec} = 0.35$. In the figure, 20 % of the detected Zn-containing ions (red) and 100% of the detected Mg ions (blue) are shown, both with a transparency $\alpha = 0.2$. These visualization parameters make quite clear the main morphological and chemical features of this heterostructure system. Notice that the exterior boundary of the reconstruction corresponds to an interior region of the tip (corresponding to the field of view of the ion detector) and hence does not match the entire projected morphology exhibited by the HAADF image presented in Fig. 2-(b).

- *Morphological and chemical features of the heterostructure*

Both QW#1 and QW#2 present the serrated profile with the groove edges aligned along the WZ *c*-axis. Their thicknesses $t_1 = (2.0 \pm 0.2)$ nm and $t_2 = (4.1 \pm 0.3)$ nm are consistent with the TEM analysis. The morphology of both is shown in detail in the magnified 5 nm-thick slices intersecting the tip axis of Fig. 3-(d,f). The same orientation of the reconstructed volume illustrates very clearly the decomposition effect within the (Mg,Zn)O barriers already discussed in the section on preliminary TEM characterization and in previous works [16,22]. This phenomenon is reproduced through the depth of the analyzed volume in Fig. 3-(c), and is also

visible in the composition maps realized on the 5 nm-thick slices intersecting the tip axis reported in Fig. 3-(e,g). This effect consists in Zn accumulation (x_{Mg} ~0.22) in correspondence of the groove edge *a*-type planes pointing towards the substrate of, while Mg is in higher concentration (x_{Mg} ~0.35) in the planes corresponding to groove edges pointing towards the epitaxial layer surface. The average composition of the barrier corresponds to a II-site Mg fraction of $\langle x_{Mg} \rangle$ = 0.27. Finally, we notice that the substrate-barrier interface, visible at the base of the reconstructed volume of Fig. 3-(c) exhibits the groove profile that is transferred to the whole heterostructure morphology during the epitaxial growth [22].

- ***PL spectra***
    - *Spectral components and energy shifts during the initial voltage ramp (constant geometry)*

The PL spectra acquired during the voltage ramp, with no evaporation (except for the last step, in which the evaporation flux was very low, $\Phi \sim 2 \times 10^{-4}$ ion/pulse), are reported in Fig. 4-(a). During this ramp the tip shape does not evolve, only the applied bias (and the surface field) change. Three spectra components can be clearly identified within the spectra. The peak at energy E = 3.34 eV is related to the ZnO substrate. It is composed by a main peak and by phonon replica at lower energy. It is not possible to exactly localize the emission, as the ZnO section illuminated by the excitation laser is around 1 µm long. The ZnO peak shifts extremely weakly during the bias ramp. It should be mentioned, however, that peak broadening towards lower energies has been found in other tip specimens from the same batch.

The asymmetric peak at E_{barr} = 3.89 eV in the unbiased tip originates from the (Mg,Zn)O barrier. Its energy is consistent with the measured barrier composition and with previous works [28,32]. It has a full width at half-maximum (FWHM) Γ_{barr} = 0.1 eV. The (Mg,Zn)O peak slightly red

shifts as a function of the applied bias, as shown quantitatively in Fig. 4-(b). The peak energy shifts from 3.90 eV to 3.85 eV during the ramp up to 6 keV. The trend of the energy also indicates a parabolic behavior rather than a linear one. The emission from the (Mg,Zn)O barrier can originate from the whole length of the tip. However, it is more likely that only the (Mg,Zn)O section below QW#1 contribute to the optical signal. This assumption is motivated by the fact that the signal of the upper QW#2 is not visible, indicating that the optical properties of the field emitter have been degraded in its upper part by the action of the FIB during specimen preparation. In any case, the (Mg,Zn)O extends over a depth of around 100 nm, which contains a sufficiently large optically active volume.

The signal of QW#1 is found at E_{QW1} = 3.462 eV in the unbiased tip. It is weak with respect to the other two peaks, but it is well defined even if it is superimposed to the high-energy tail of the ZnO peak. The inset in Fig. 4-(a) underlines the details of the peak red shift when V_{DC} increases. The evolution of the peak energy is reported in Fig. 4-(b) as a function of the bias. Similarly to the case of the (Mg,Zn)O peak, the QW#1 peak gradually shifts from 3.462 eV to 3.443 eV. The FWHM remains close to the unbiased value Γ_{QW1} = 20 meV. What is crucial about the QW#1 signal is that its emission can be very precisely localized within the 2 nm of its layer thickness. This makes the QW#1 a local optical probe for the environmental parameters that can influence its optical signature during the experiment.

All peak intensities remain constant throughout the initial bias ramp.

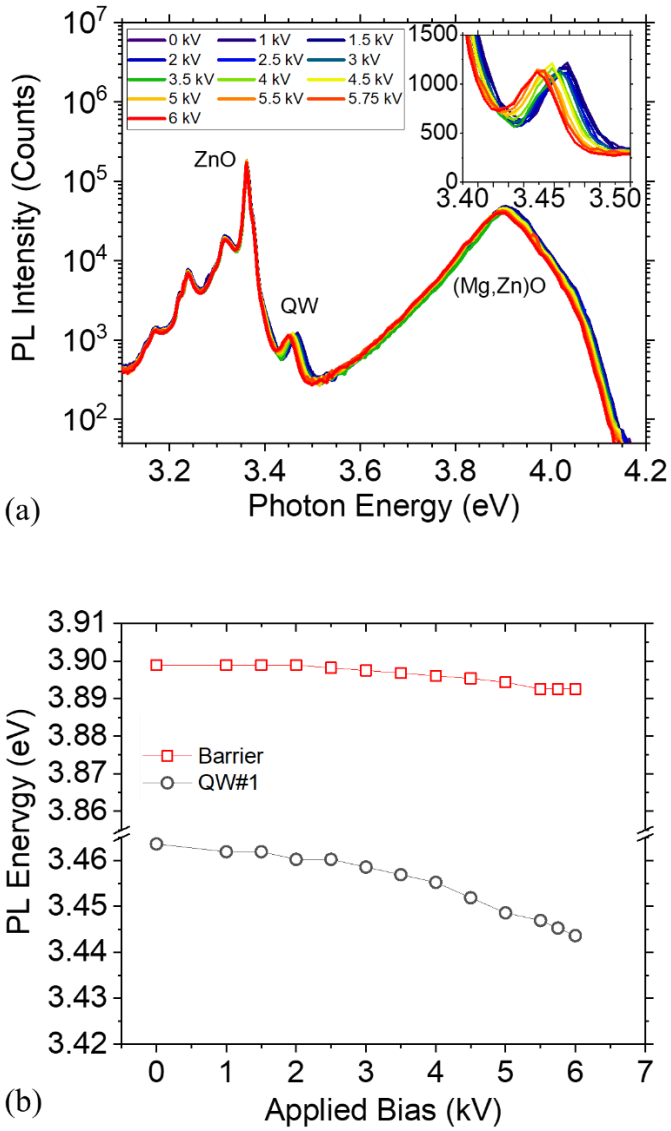

Fig. 4 Photoluminescence of the analyzed field emitter during the initial bias ramp. The tip shape is not changing as no evaporation takes place. (a) PL spectra. The inset is a close up of the QW#1 luminescence. (b) Peak energies of the emissions of the (Mg,Zn)O barrier (red squares) and of the QW#1 (black circles) reported as a function of the voltage applied to the tip V_{DC}.

- *Energy shifts during the evaporation (quasi-constant field)*

The evolution of the PL spectra during the specimen evaporation and the relationship between the PL spectrum index i_{PL} and the reconstructed APT volume are shown in Fig.-5-(a,b), while part (c) is a zoom of the QW#1 spectral region. The series of PL spectra is shown here as a 2D color plot, which better allows following the energy trends along the experiment.

Referring to Fig.-5-(b) and from the plot of Fig.-5-(d) in which the maximum energies of the (Mg,Zn)O and QW#1 peaks are reported as a function of i_{PL}, it is clear that the energies of both peaks evolve during the analysis. The energy of QW#1 steadily decreases, with the exception of a local increase after i_{PL} = 60. The local blue shift that both peaks experience at i_{PL} = 60 well correlates with the local decrease of V_{DC} and of the surface electric field corresponding to the evaporation of QW#2, as reported in Fig. 3-(b). The occurrence of this local blue shift will be explained in detail in the discussion section. The energy of the barrier emission also exhibits changes, but as this emission is due to the superposition of dipoles distributed along tens of nanometers, its interpretation is not straightforward.

Focusing on the QW#1 emission, the plot in Fig. 5-(d) shows that its maximum energy changes from E = 3.445 eV at the beginning of the evaporation to E=3.425 eV shortly before the evaporation of QW#1: the peak undergoes thus a red shift of ΔE_1 = -20 meV through the analysis (the shift of the average being slightly lower due to the superposition of the ZnO peak tail). The total red shift from the beginning of the voltage ramp amounts altogether to ΔE_1 = -30 meV. The PL of QW#1 is completely suppressed for i_{PL} = 88. Comparison with the reconstructed volume show in Fig.-5-(b) indicates that the loss of PL signal takes place when the apex is at the maximum distance of around 10 nm from the QW#1 region. This could be due either to the fact that the actual emitting dipoles are not close to the axis in the APT field of view or to the increase of stress at the proximity of the apex – to be quantified in the following - which may induce the migration of non-radiative point defects towards the QW#1.

It should be noticed that both (Mg,Zn)O and QW#1 peak intensities vary throughout the analysis. This behavior is most likely related to the shape evolution of the field emitter and to the variation of the dielectric environment of the emitting dipoles. However, this phenomenon constitutes *per se* the object of a different study and will not be treated in this work.

The energy shifts of the PL emission can be interpreted through the effect of strain within the field emitter. This requires first to set down the theory of strain within a field emitter in an electrostatic field, which constitutes the focus of the next section.

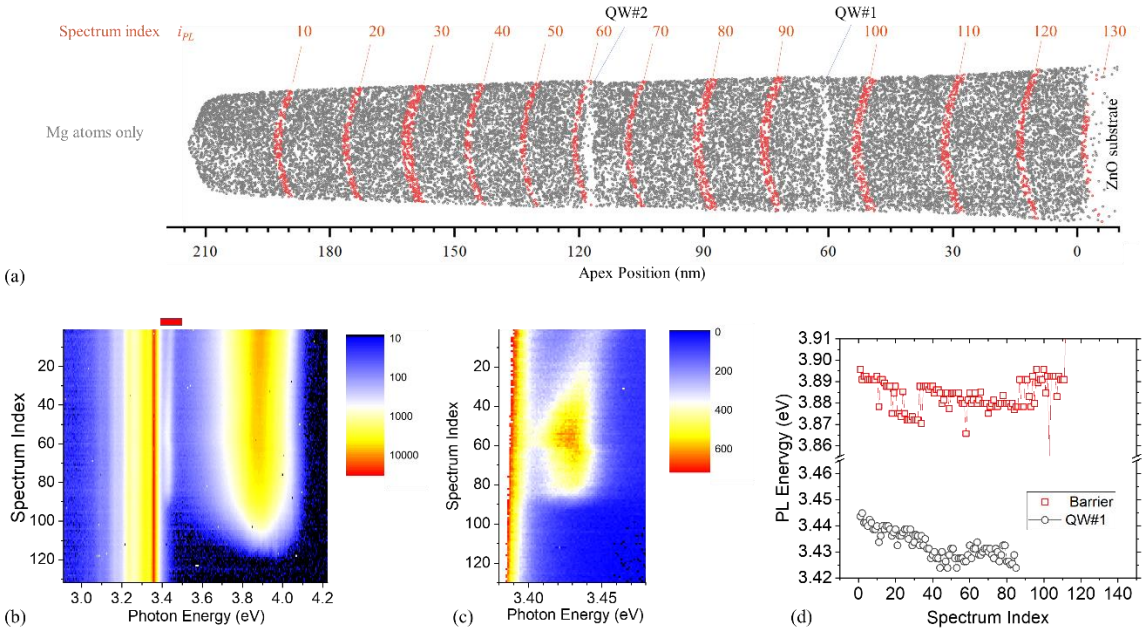

Fig. 5 (a) Slice extracted from the 3D reconstruction of the positions of the Mg ions. The ions highlighted in orange correspond to those detected during the acquisition of the PL spectrum indexed by i_{PL}. (Notice that only the volumes collected during the 10th, 20th, 30th, etc. Spectra are shown in this way and serve as a reference for the eye) (b) Sequence of the PL spectra acquired during the evaporation of the field emitter. The red bar indicates the spectral region corresponding to the QW#1 emission, i.e. to the close up shown in (c). (d) PL energy of the (Mg,Zn)O barrier (red squares) and of the QW#1 (black circles) as a function of the spectrum index i_{PL}.

IV. STRESS, STRAIN AND BANDGAP EVOLUTION IN AN EVAPORATING FIELD EMITTER

These experimental results can be interpreted through the theory of linear elasticity in semiconductors and through strain-dependent band theory [33]. While this theory has already proven to be useful in the study of nanowires [14,34], it has not been applied, so far, to field emitters which change shape during evaporation. This constitutes the object of the present section.

Stress and strain may build up in a field emitter via two distinct mechanisms:

i) *A structural mechanism*, i.e. the presence of built-in strain due to the presence of coherent heterostructure interfaces. Due to the nanoscale dimensions of the system, this built-in strain can elastically relax at the field emitter surfaces. Relaxation is more effective when the lateral dimensions of the tips are smaller, i.e. the phenomenon depends on the geometric shape of the system. A similar situation is found in nanowire axial [35] and radial [36] heterostructures.

ii) *An environmental mechanism*, i.e. the application of an electrostatic potential at the tip, translating into an electrostatic field at the tip apex. This field induces an electrostatic stress that propagates into the tip volume in a way that depends on its geometric shape [26].

For the sake of clarity, we make in the following three simplifying assumptions:

a) The strain-related energy shifts observable in the exciton recombination yielding the PL signal of the quantum well are determined by the action of strain on the ZnO bands only. In other words, we assume that strain affects the recombination energy via its effect on the bandgap energy of the highest valence bands (or, equivalently, on the lowest exciton energy). The possible effect on the alignment of the ZnO and (Mg,Zn)O bands has been

shown to be negligible [22]. The effect on the QW confinement energy is also expected to be negligible versus the bandgap shift.

b) The ZnO/(Mg,Zn)O QW/barrier system can be described as a set of planar interfaces between homogeneous phases. Despite APT clearly shows that this is not the case, as the QW/barrier interface has a groove profile and decomposition phenomena take place within the barriers, this approximation can be shown to be tenable. We will indeed show in the following that the main agent responsible of the PL energy shift of the QW observed during the PAP analysis is the applied electric field. Furthermore, the effect of the decomposition in (Mg,Zn)O would only result in some dispersion of strain and stress values in the neighborhood of the same trends that a random alloy would exhibit.

c) The optically active region lies close to the axis of the field emitter. This assumption is justified by the fact that FIB preparation introduces non-radiative recombination centers over a distance of several tens of nanometers from the surface [37]. The interpretation of the experimental results is then performed based on the quantities calculated along the axis of the field emitter.

- ***General relationships***

The stress and strain tensors $\overleftrightarrow{\sigma}$ and $\overleftrightarrow{\varepsilon}$ are linearly dependent via the stiffness matrix *C* containing the elastic constants of the material:

$$\overleftrightarrow{\sigma} = C\overleftrightarrow{\varepsilon}. \qquad (1)$$

The numerical values of the elastic constants relative to ZnO and (Mg,Zn)O are given in the Appendix.

The effect of strain on the band energies can be determined by solving the eigenvalue problem of the **k·p** effective mass Hamiltonian at the Γ point of the Brillouin zone, defined in the quasicubic model for II-VI wurtzite semiconductors [33], also adopted in refs. [38,39]:

$H = H(\overleftrightarrow{\varepsilon})$.

The strain-induced energy shift is then calculated as the variation of the energy gap of the ZnO with respect to its strain-free state. Notice that this does not consider the effect of strain on the confinement energy. This approximation will be justified *a posteriori* in the section dealing with the limitations of the model.

As recalled in more detail within the Appendix, the strain Hamiltonian contains both constant terms relative to the unperturbed band structure and strain-dependent terms. These are determined by the set of deformation potentials of ZnO [33,38]. It should be noticed that a corresponding set of deformation potentials has not been determined yet for (Mg,Zn)O with arbitrary Mg content.

It must also be underlined that stress and strain are linearly dependent, so the components of the strain tensor induced by an electrostatic stress adds up to the components related to lattice mismatch or surface relaxation. However, the eigenvalues of the $H(\overleftrightarrow{\varepsilon})$ Hamiltonian are in general not linearly dependent on the strain components. It is thus the total strain that must be fed into $H(\overleftrightarrow{\varepsilon})$ in order to accurately calculate the energy shift resulting from the superposition of different stress or strain sources.

- ***Lattice mismatch-induced strain***

In a ZnO quantum well grown epitaxially on the m-plane, strain can build up due to lattice mismatch along the a- and the c- axis (here identified with the y and z direction, respectively). If the ε_{yy} and $\varepsilon_{zz}$of the strain tensor are given, the on-axis component ε_{xx} is then found by

$$\varepsilon_{xx} = -\frac{c_{12}\varepsilon_{yy}+c_{13}\varepsilon_{zz}}{c_{11}} \qquad (2)$$

Where the c_{ij} are the components of the stiffness matrix *C*. Keeping this relationship into account, the expected shift of the lowest exciton energy E_1 is visualized in the plot of Fig. 6-(a). However, the strain relationship for a ZnO QW epitaxially grown on (Mg,Zn)O must comply with specific constraints.

ZnO and (Mg,Zn)O do not possess the same lattice constants. Under the hypothesis that there are no decomposition or phase separation phenomena in (Mg,Zn)O, the lattice constants can be expressed as a function of the II-site Mg fraction x_{Mg} as follows [40]:$a(x_{Mg}) = (3.2459 + 0.012\, x_{Mg} + 0.09\, x_{Mg}^2)$ Å (3)

$$c(x_{Mg}) = (5.2126 - 0.076\, x_{Mg} - 0.142\, x_{Mg}^2)\ \text{Å} \qquad (4)$$

It is remarkable that in (Mg,Zn)O the lattice is deformed in a highly anisotropic way, as it expands on the basal plane and it contracts along the polar c-axis of the wurtzite with increasing Mg content. In the present work, the ZnO/(Mg,Zn)O interfaces are approximately defined along the *m*-plane. A coherent ZnO/(Mg,Zn)O interface is therefore characterized by strains of opposite signs along the *y* and *z* (i.e. *a*- and *c*- in the WZ system) directions on the plane. According to relations (3) and (4), a ZnO QW coherently strained on relaxed (Mg,Zn)O with $x_{Mg} < 0.32$ has a strain state spanning the black line traced in the plot of Fig. 6-(a).

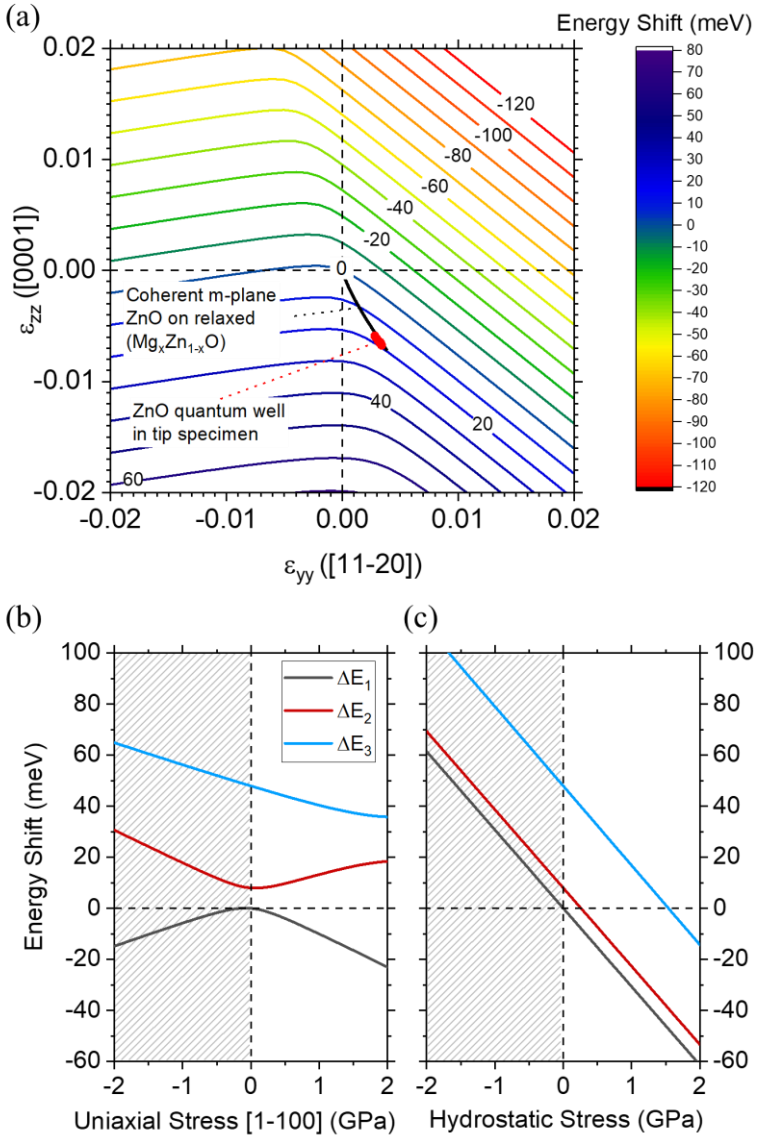

Fig. 6 Strain and stress effects on the exciton energies in ZnO. (a) Relationship between the in-plane strain tensors of a coherently strained ZnO film epitaxially grown on the m-plane and the energy shift of the lowest exciton level. The black line represents the strain state of a coherent m-plane ZnO layer epitaxially grown on relaxed $Mg_xZn_{1-x}O$ ($x < 0.35$). The red spot indicates the strain state calculated for the ZnO QW contained within the field emission tip. (b) Energy shifts of the three ZnO exciton bands as a function of a uniaxial stress directed along the m-direction [1-100]. (c) Energy shift of the three ZnO exciton levels as a function of the hydrostatic stress. The grey-shaded regions correspond to compressive stress, not applicable in the present experiment.

- *Properties in a tip with constant shape*

The thin film samples grown by MBE for this study have been designed in order to support a pseudomorphic growth of the (Mg,Zn)O layer. In other words, (Mg,Zn)O acquires the same lattice constants of ZnO on the *m*-plane and it slightly adapts its lattice constant along the m-axis in order to minimize the elastic energy. In this pseudomorphic thin film configuration, the ZnO QWs have thus the same lattice parameters of the ZnO substrate and the bandgap shift would be zero.

The results of the strain calculation performed within the elastic energy minimization algorithm implemented by the Nextnano^{++} solver [41] on the geometry of the studied tip and reported in Fig. 7-(a,b) for the tip before evaporation shows that the situation is radically different in field emitters. In the studied system, the interlayer distance and the extension of the region of interest are comparable with the radius of the cross section of the tip. In this situation, strain relaxes effectively at lateral surfaces. The (Mg,Zn)O barrier is strained on ZnO (actually only partially, as it mutually strains the ZnO substrate), but it relaxes to its unperturbed lattice parameters between QW#1 and QW#2. QW#1 is thus very close to the situation of ZnO coherently strained on relaxed (Mg,Zn)O. The stress state is calculated through the application of eq. (1) to the strain maps, and is reported in Fig. 7-(a,b), showing that stresses of the order of the GPa can build up along the interface planes. Consistently with the (3)-(4) relations, ε_{yy} and σ_{yy} are positive, while ε_{zz} and σ_{zz} are negative. As the tip is free to relax in the *x* direction, the σ_{xx} component of the stress tensor is nearly zero. The energy shift of the lowest exciton level is calculated by applying the $H(\overleftrightarrow{\varepsilon})$ Hamiltonian on the strain maps and is reported in Fig. 7-(d). The exciton energy in the QW#1 undergoes a blue shift of around 16 meV.

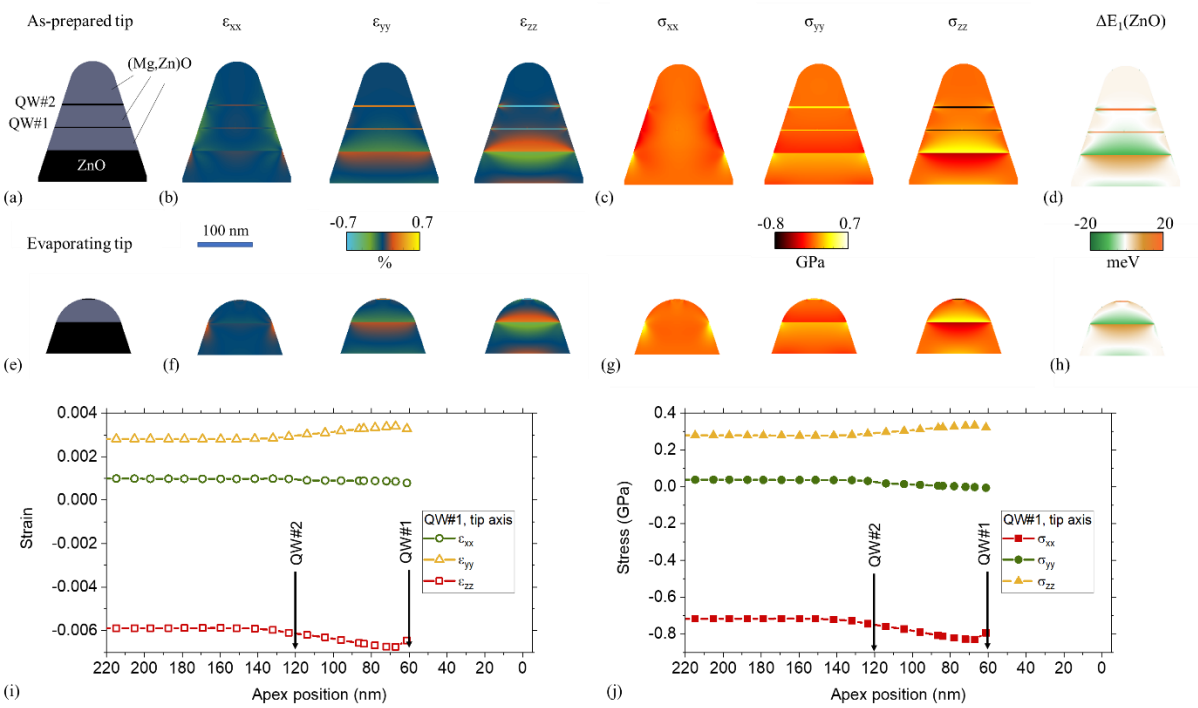

Fig. 7. Strain/stress states related to lattice mismatch and their evolution in the field emitter containing the ZnO/(Mg,Zn)O heterostructure. (a-d) Field emitter before evaporation: (a) Scheme of the materials system (b) components of the strain tensor (c) components of the stress tensor (d) expected shift of the lowest ZnO exciton level. (e-h) correspond to (a-d) for the situation in which the apex of the field emitter is in close proximity with the QW#1 after partial evaporation. (i) Evolution of the strain components at the center of the QW#1 as a function of the apex position. (h) Evolution of the stress components at the center of the QW#1 as a function of the apex position.

- *Evolution of stress, strain and bandgaps in an evaporating tip*

When the field emitter evaporates, its shape gradually transforms into that schematically shown in Fig. 7-(d). This is a sort of snapshot of the tip shape just before the evaporation of QW#1. The strain and stress components for this configuration are visualized in the 2D color plots of Fig. 7-(d). What can be noticed from these plots is that the strain due to the lattice mismatch at the ZnO substrate/MgZnO interface relaxes more effectively due to the modified shape of the tip. As a result, QW#1 will be lying on an almost completely relaxed (Mg,Zn)O. The strain and

stress state at the center of the QW#1 varies as a consequence of this relaxation and is quantitatively reported in Fig. 7-(i). From both strain and stress trends it appears that the variation of the strain and stress state is small but not negligible. The relative change in the strain or stress state for the *yy* and *zz* in-plane components may be up to 20 % through the experiment. The in-plane strain state of the QW#1 is also reported in the red spot in Fig. 6-(a). Interestingly, the modification begins to take effectively place upon the evaporation of the upper QW#2, which is reasonable as any ZnO inclusion within the (Mg,Zn)O matrix has the effect of inhibiting the relaxation of the latter. If we neglect the effect of the applied bias (which will be treated in the next section), the energy shift of the lowest exciton energy varies from 16 meV to 19 meV as reported through the blue dotted line of Fig. 8.

As a concluding remark for this section, these results are related to the tip geometry, to the heterostructure configuration, and to the crystal orientation specific to this study. Calculations performed on other tip geometries – not shown – indicate that the modification of the energy shift decreases with decreasing tip radius, which may be easily understood as due to the proximity of the lateral surfaces assisting the relaxation of the (Mg,Zn)O lattice at short distance from the interface with the ZnO substrate. Considering all these parameters, the effect of lattice relaxation during tip evaporation may thus be larger in other systems.

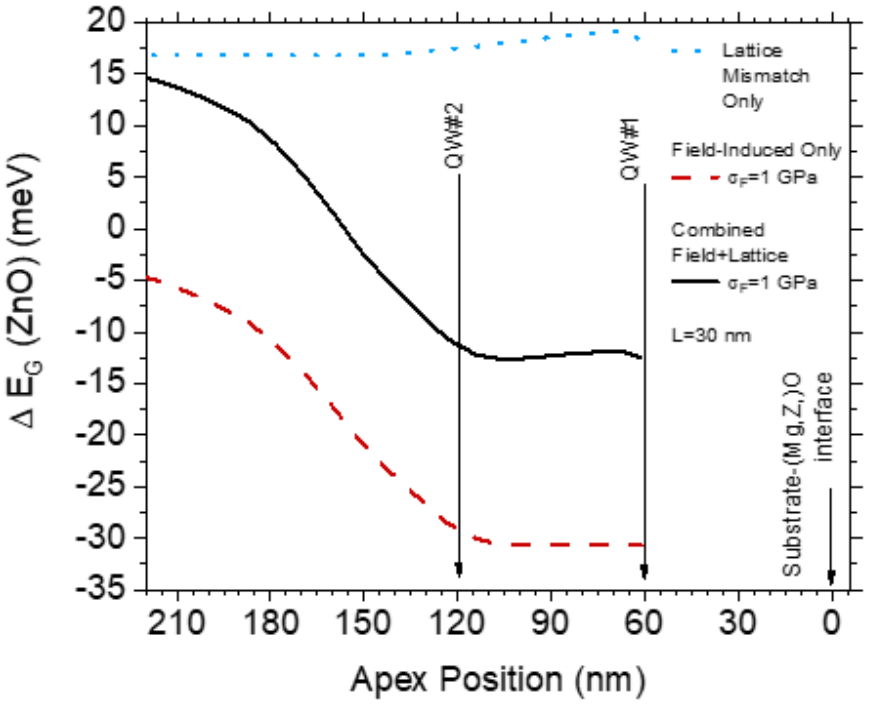

Fig. 8 Energy shifts calculated as a function of the apex position in the evaporating field emitter. Blue dotted line: shift related to the lattice mismatch, neglecting the effect of the applied field. Red dashed line: shift related to the applied bias, neglecting the effect of the lattice mismatch. Black solid line: shift resulting from the combined effect of lattice mismatch and applied bias.

- ***Field-induced strain***

The problem of the stress induced by the voltage applied to a field emission tip has been thoroughly discussed in a previous work [26]. The intensity of the electric field F_s present at the apex surface can be related to the apex radius R_{apex} of the needle and to the applied bias V_{DC}:

$$F_s = \frac{V_{DC}}{k_f R_{apex}} \qquad (5)$$

where k_f is a geometric factor depending on the tip shank angle and on its electrostatic environment [42]. Due to the accumulation of a high density of valence band holes on the apex surface [43], the field induces a Maxwell stress on the apex surface:

$$\sigma_F = \frac{1}{2}\varepsilon_0 F_s^2 \qquad (6)$$

At constant geometry, the apex stress (and the linearly related strain) is thus proportional to the square of the field and, through eq. (5), to the square of the applied voltage. Concerning the electric field, we assume that it can be considered as completely screened in the tip within the first nanometer from the surface, as supported by the calculations and the experimental observations reported in ref. [43].

- *Properties in a tip with constant shape*

Approximating the apex as a hemisphere and integrating the forces $d\boldsymbol{T}$ that develop on a surface element dS, the resultant tension $\boldsymbol{T}$ along the needle axis is

$$\boldsymbol{T} = \pi R_{apex}^2 \sigma_F \hat{\boldsymbol{n}}_{[\mathbf{1-100}]} \qquad (7)$$

where $\hat{\boldsymbol{n}}_{[\mathbf{1-100}]}$ is a unit vector pointing along the [1-100] crystal direction aligned with the tip axis for the particular system studied in this work. The stress at the apex itself is hydrostatic, as the Maxwell forces are directed approximately along the needle radius. At a distance from the apex equal to several R_{apex}, there is a transition from hydrostatic to uniaxial stress acting on an axial cross section of the tip is uniaxial. This transition is described in an analytic approximation as follows:

$$\sigma_{xx}(x) = |\boldsymbol{T}|/S(x), \qquad (8)$$

$$\sigma_{yy}(x) = \sigma_{zz}(x) = \sigma_{xx}(x)\exp((x - x_i)/L)$$

where

$$S(x) = \pi \cdot R(x)^2 \qquad (9)$$

is the area of the axial cross section at the coordinate x, and x_i is the coordinate of the interface between the hemispherical and the conical section of the tip. The coordinate x_i decreases as the evaporation progresses. The transition length L is a priori not known, because it depends not only on the geometry of the tip but also on the actual value of the field on the conical section, which is non-zero. In principle, the field could be calculated everywhere on the tip, then the stress could be calculated with, e.g. a finite element approach. However, this approach is more complex and would be less transparent than the adopted analytical approximation. The transition length L can in any case be treated as a sort of fitting parameter, as will be shown in the discussion section. The strain state is then calculated by the application of the inverse of the C matrix (eq. (1)) on the stress maps. The trends of strain and stress components in the actual tip geometry are reported in fig. 9-(b,c), respectively, for an apex stress of $\sigma_F = 1$ GPa. The maps are traced for a transition length L = 50 nm, which is of the order of the apex radius before the evaporation. This value is unrealistically small, but it is suitable for visualization purposes.

The effect of uniaxial stress directed along the m-axis and that of a hydrostatic stress on the exciton energies are reported in Fig. 6-(b) and –(c), showing that for an apex tensile stress strength of 1 GPa red shifts of around -10 and -30 meV are expected in the case of the uniaxial and hydrostatic stress, respectively. The energy shift in the tip geometry, calculated with the $H(\varepsilon)$ Hamiltonian, is reported in Fig. 9-(d). The apex stress induces a red shift of around -30 meV in the proximity of the apex (i.e. in the region included in the hemispherical region close to the apex) where the stress is hydrostatic. The exciton energy shift, calculated in the absence of the lattice mismatch-related effects, gradually decreases towards the interior of the tip due to the increase of its cross section and to the transition to uniaxial stress.

For a tip with constant geometry, the strain/stress relationships are linear. So, in every point of the tip, stress and strain are proportional to the square of the surface field F_s and of the applied voltage V_{DC}.

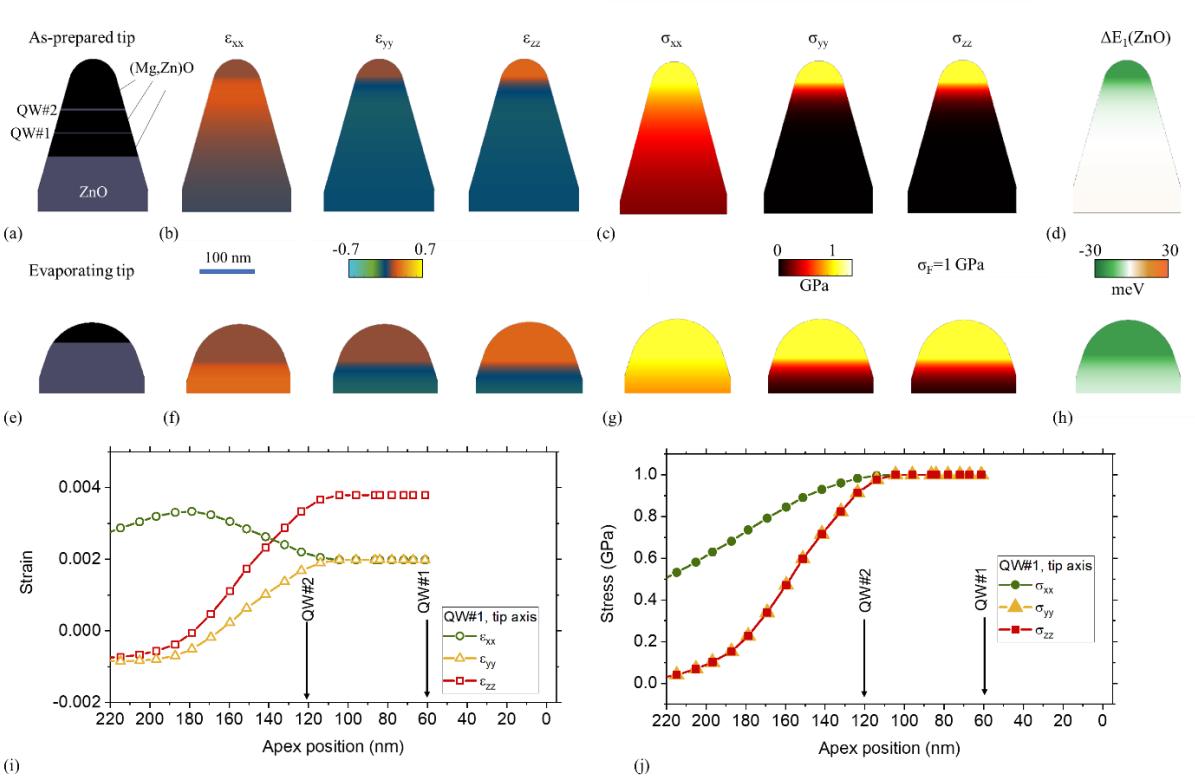

Fig. 9. Strain/stress states related to the application of an electric field at the apex and their evolution in the field emitter containing the ZnO/(Mg,Zn)O heterostructure. The apex stress is set at 1GPa while the hydrostatic/uniaxial stress transition length L is set at L= 30 nm. (a-d) Field emitter before evaporation: (a) Scheme of the materials system (b) components of the strain tensor (c) components of the stress tensor (d) expected shift of the lowest ZnO exciton level. (e-h) correspond to (a-d) for the situation in which the apex of the field emitter is in close proximity with the QW#1 after partial evaporation. (i) Evolution of the strain components at the center of the QW#1 as a function of the apex position. (h) Evolution of the stress components at the center of the QW#1 as a function of the apex position.

- *Evolution of stress, strain and bandgaps in an evaporating tip*

The components of the stress tensor induced at the center of QW#1 by a constant electric field applied to the tip apex are reported in Fig. 9-(c) as a function of the distance of the apex from the (Mg,Zn)O/ZnO substrate interface for the tip structure shown in Fig. 9-(a). The corresponding components of the strain tensor at the center of QW#1 are visualized in Fig. 9-

(b). These plots illustrate the dynamical evolution of the mechanical state of the QW#1 during the evaporation of the tip.

The reported data indicate that the strain induced by the applied field within the QW#1 increases as the apex approaches. This happens because the applied field remains constant (approximately constant in the actual experiment) but it is applied to a larger and larger apex as the tip evaporates. In this way, the total mechanical tension on the tip increases during its evaporation. It should be noticed that the largest strain component is the ε_{xx} when the stress is uniaxial, while it becomes the ε_{zz} when the stress becomes hydrostatic close to the tip apex.

The expected energy shift on the lowest exciton energy, calculated without considering any other strain sources, is reported as the red dashed line in Fig. 8 for an apex stress σ_F =1 GPa, corresponding to an apex field of F_s = 15V/nm. The shift varies from around -8 meV to around -30 meV from the beginning of the experiment to the evaporation of the QW#1 layer. At this apex stress strength, the effect of the field-induced stress and its modification during evaporation are significantly larger than the energy modification related to the relaxation of the lattice during evaporation.

- ***Combined effect of lattice mismatch-related and field-induced band shifts***

The combined effect of lattice mismatch-related and field-induced shift of the lowest exciton energy is shown by the black solid line in Fig. 8 for an assumed apex stress = 1 GPa and a transition length L = 30 nm. The energy shift resulting from the combination of the two mechanisms is not exactly the linear combination of the two separately considered shifts, but it is quite close to it. It can be noticed that the trend of the combined shift qualitatively reproduces the trend of the energy shift related to the effect of the field during evaporation. The lowest exciton energy undergoes indeed a shift varying from 15 meV to -11 meV.

V. CORRELATION OF MODEL AND EXPERIMENT

- ***Interpretation of the energy shifts of the quantum well luminescence***
    - *Determination of apex stress and electric field*

The shift observed in the PL energy of QW#1 can be interpreted as due to its varying strain state both as a function of the applied voltage when its geometry is constant and as a function of the evaporated volume while it is evaporating during APT analysis. The model developed in the previous section allows us calculating the expected spectral shifts on the actual tip geometry.

Figure 10-(a-d) represent a synthetic view of the experimental data of the peak energy of the QW#1 (a,c) as a function of the applied bias during the voltage ramp (b,d) and as a function of the apex position during the evaporation. In Fig. 10-(a,b) the experimental data are compared with the predictions of the calculation for different values of the apex stress σ_F and with a fixed hydrostatic/uniaxial stress transition length L=150 nm. The position of the calculated shift with zero stress is translated on the energy scale in order to match the PL energy of the unperturbed QW#1 (i.e. contained in the tip when V_{DC}=0).

In part (a), the experimental data are compared with the calculation of the expected shift at the QW#1 when an increasing stress ${\sigma_F}^{ramp}(V_{DC})$ is applied during the voltage ramp. This stress then stabilizes at σ_F.The relationship between the stress ${\sigma_F}^{ramp}$ and the voltage is simply given by

$${\sigma_F}^{ramp}(V_{DC}) = \sigma_F \left(\frac{V_{DC}}{V_{e,s}}\right)^2 \quad (10)$$

Where $V_{e,s}$ = 6 kV is the voltage where evaporation "starts", i.e. yields the detection rate set for the experiment. In part (b) the PL energy during evaporation can be compared with the different shifts expected for different apex stress. Considering both voltage ramp and evaporation, it is

apparent that the best approximation of the overall shift (i.e. from the absence of field to the situation in which the QW#1 is close to evaporation) is given by the assumption of an apex stress of σ_F = 1.25 GPa. This value corresponds to an apex surface field F_s = 16.8 V/nm, which is very close to the value assumed for the reconstruction algorithm, and which is consistent with the microscopic field value of $F_\mu \sim 20$ V/nm inferred from the charge state analysis. We notice, however, that for σ_F = 1.25 GPa and L = 150 nm the PL behavior during the ramp is not best reproduced. The ramp is best fitted by the parabola with σ_F = 1.5 GPa. However, this stress value predicts a larger red shift than experimentally observed. This apparent discrepancy is related to the assumption about the hydrostatic/uniaxial stress transition length.

The effect of the hydrostatic/uniaxial stress transition length L is shown in Fig. 10-(c,d). The different calculated curves relate to an apex stress during evaporation σ_F = 1.25 GPa, while L is allowed to vary. It appears clearly that the curves best fit the PL shift during the voltage ramp in (c) when L > 200 nm, i.e. assuming a hydrostatic stress reaching the QW#1. It is clear that, for values of L larger than the actual QW#1 distance from the apex at the beginning of the evaporation, the strain state only weakly depends on L at the QW#1 position. It is thus not possible to draw a quantitative conclusion about L, but a lower limit L = 200 nm can be set. This behavior is most probably related to the presence of a residual surface field at the surface of the conical part of the tip, a field which is not sufficiently intense for promoting evaporation, but which still has non-negligible mechanical effects. It can also be underlined that this conclusion is consistent with the results obtained in a previous works, in which the splitting of the zero-phonon lines of the PL of color centers in diamond were studied [26,27]. In these works, it was possible to measure the apex stress under the hypothesis that the stress was uniaxial. In these studies, the distances of the emitting centers from the apex were significantly larger, up to several microns, so that it would not be reasonable to expect a hydrostatic stress.

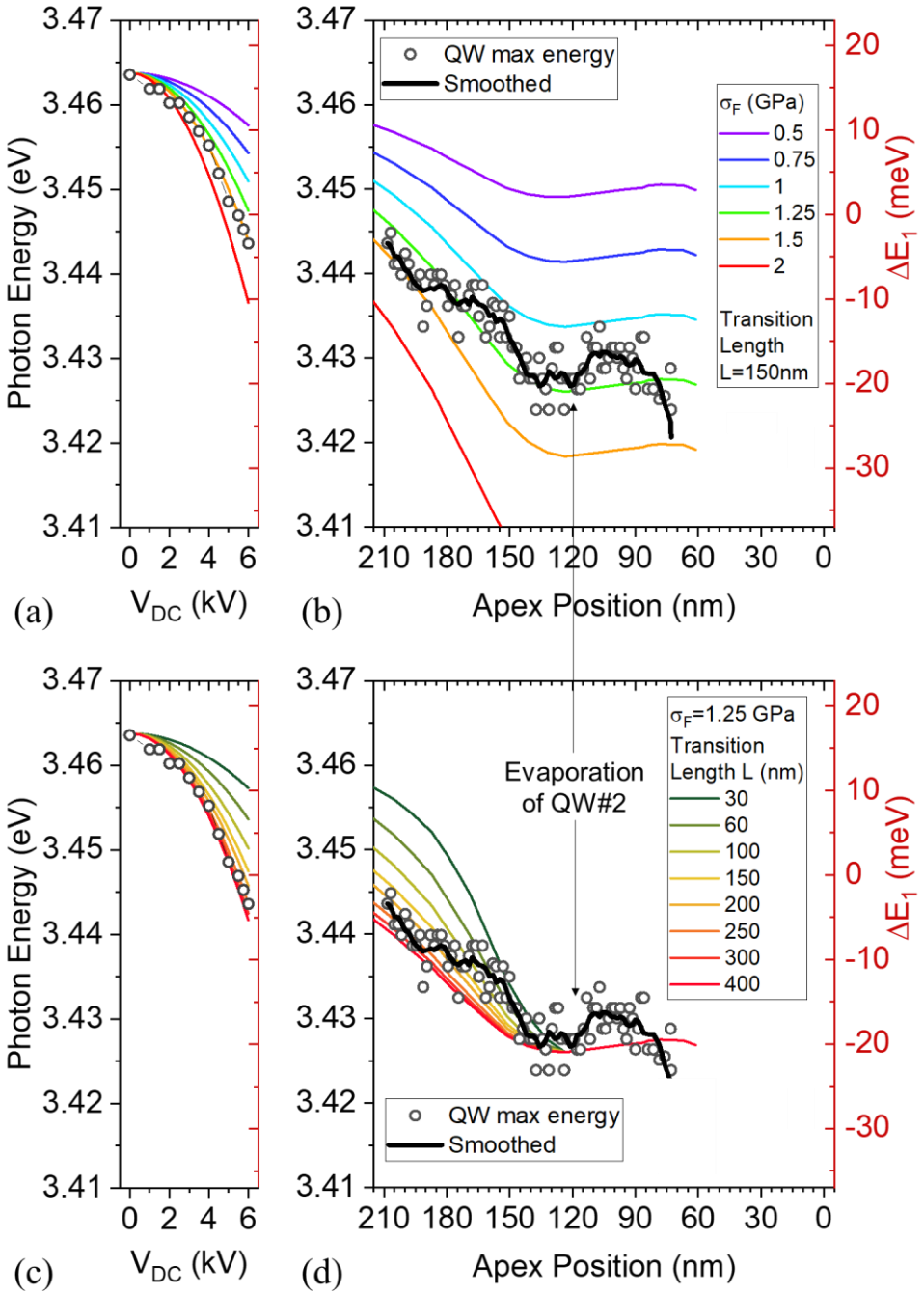

Fig. 10 Comparison between the calculated and the experimental energy shifts. (a) Experimental and calculated PL energies during the voltage ramp as a function of the applied bias V_{DC} and (b) as a function of the apex position during the field emitter evaporation calculated for different apex stress levels and for a fixed hydrostatic/uniaxial stress transition length L=150 nm. (c,d) Same as in (a,b), but the calculations are performed for a fixed apex stress σ_F=1.25 GPa and for varying values of L.

- *Optical sensing of field variation*

The calculations performed according to the model do not consider the variation in the surface field which occurs when the QW#2 is evaporated. This variation will be now discussed in more detail. According to the voltage curve (Fig. 3-(b)), the relative difference in the applied voltage implies a similar relative difference in the surface field, $|\Delta V_{DC}/V_{DC}| = |\Delta F_s/F_s| \approx -4$ % during the evaporation of QW#2. Comparing the local increase in the QW#1 PL energy with the calculations reported in Fig. 10-(b), we can estimate that just after the evaporation of QW#2 the stress decreased from 1.25 GPa to around 1.1-1.15 GPa, with a relative difference $|\Delta\sigma_F/\sigma_F| \approx$ 12-8 %, which is reasonably close to the expected value $|\Delta\sigma_F/\sigma_F| \approx 2|\Delta F_s/F_s|$ expected from the quadratic relation (6).

The important point about this phenomenon is that QW#1 *senses* the evaporation of QW#2. The use of a PAP makes it possible to establish a sort of strain coupling of these two wells via the action of the surface electric field. The evaporation of the QW#2 leaves a trace on the behavior of QW#1. Clearly, this also depends on the fact that the experiment is set at constant detection rate. However, it is possible to imagine that closer QWs would exhibit a stronger strain interaction: this would be related to the relaxation of the lattice-related strain during evaporation, because the amount of evaporated volume of the upper-lying QW would have a larger impact on the strain state of the lower-lying QW. This opens up interesting possibilities for the study of the optical properties of quantum confined emitters by PAP.

Finally, it is worth mentioning that the mechanical tension on the tip increases during its evaporation. Also, the stress exerted at the base of the tip, where it is usually soldered to a larger tip-shaped support, increases during the experiment. If the base is not sufficiently large or properly soldered, this increase may be at the origin of specimen failure in APT analysis of soldered specimens, analyzed with approximately constant surface field through the experiment.

- ***Limitations of the current approach***

In order to conclude the discussion section, it is worth clarifying the main limitations of the results presented in this work. There are indeed both experimental and theoretical limitations that can be possibly overcome in the next future.

  - *Experimental limitations*

From the experimental point of view, the current setup is limited to a geometrical field of view of the ion detector of around ±8°. This makes it possible to image a quantum well within a heterostructure at the correct depth, but it excludes a large part of its volume. As carrier localization is an important phenomenon in these systems [44–46], carriers may localize outside the field of view of the APT. This may also be the reason why the QW#1 luminescence quenches some 10 nm before the apex reaches it on the axis, i.e. before it completely evaporates. This limit can be relaxed through a technical intervention on the instrument. Increasing the field of view will be highly beneficial for the study of point-like light emitters such as quantum dots (QDs) or color centers. Deeper insight can indeed be reached if it will be possible to compare the full 3D chemical image of the light emitter with its optical signature. Another point concerns the effective measurement of tip shape, which is known to deviate from that of a cone surmounted by a portion of sphere or ellipsoid in the case of evaporation of layers with significantly different evaporation fields [47] – this possibility may apply to specific QW systems. It would be interesting to exactly know the shape of the tip (particularly its apex radius) during the evaporation. This would require a much more demanding approach, with the implementation of a PAP coupled with a transmission electron microscope.

Finally, we notice that the electrostatic stress can be applied as a tensile stress only (changing the sign of the bias would not change the sign of the stress, not to mention that electron field emission would set on well before reaching the field intensities typical of ion emission). However, the method presented here is an original way to implement tensile strain-dependent measurements not only on top-down fabricated field emitters, but also on nanowires, which can be characterized by APT based on different preparation protocols [48]. An original optical path to strain-stress curves on nanoscale systems can be considered as opened.

- *Limitations of the model*

In this work we chose to perform calculations within a simplified theoretical framework, meant to convey the novelty of the results and the interplay of different physical aspects of the analyzed system. Among the main simplifying assumptions, we adopted several ones about the strain model, in particular the adoption of an analytical approximation in order to describe the stress propagation within a field emitter. This limitation can be overcome by implementing finite element calculations similar to those carried out for the lattice-mismatch related stress (it should be mentioned that the solution of the stress/strain equations given boundary conditions at the tip surface is not implemented in the software package we used; furthermore, the determination of such boundary conditions is *per se* another problem [47]). The exciton energy shift was calculated only based on the strain effect on the ZnO bandgap. The effect on the (Mg,Zn)O bandgap is more difficult to determine because the deformation potentials for this material are not as well-known as for ZnO. More precise calculations could be achieved by considering the quantum confinement effect, and possibly the wavefunction symmetry. However, these calculations would be probably more precise, but it is likely that the effect of the evolution of the strain state on the confinement energies would not be particularly significant. Concerning the effect of the strain on the confinement energy, for instance, we

consider that the shift ΔE_g of the ZnO bandgap spans over around 30 meV, yielding a relative shift $\Delta E_g/E_g \sim 1\%$. A similar relative shift should set on for the QW confinement energy i.e. $\Delta E_{c,QW}/ E_{c,QW} \sim 1\%$. As $E_{c,QW}$=0.1 eV, this would correspond to a shift of the confinement energy of around $\Delta E_{c,QW} \sim 1$ meV , which is lower than the level of fluctuation of the peak energy during the analysis. The field-induced variation of the strain state could also lead to modifications of the wavefunction symmetry (such modifications are here somehow embedded in the strain dependence of the valence bands in the **k·p** Hamiltonian, but this Hamiltonian refers to bulk properties, and quantum confinement effects could occur in the case of narrow QWs). Finally, an estimate – or a measurement – of the effective temperature of the quantum well would add useful information, also in terms of possible effects of the differences of lattice expansion of the heterostructure phases. These implementations are left for further and more specialized work.

VI. CONCLUSIONS AND PERSPECTIVES

In summary, this work reports on the possibility of measuring stress, strain and the intensity of the field applied to the apex of a field emitter through the application of a recently developed instrument, referred to as photonic atom probe (PAP), coupling atom probe tomography (APT) and photoluminescence (PL) spectroscopy. We applied this correlative technique to the analysis of ZnO/(Mg,Zn)O quantum well heterostructures. The PL signal of a QW was found to shift in energy as a function of the voltage applied to the field emitter. In order to explain this shift, we developed a strain model keeping into account the crystal orientation of the emitter, the dimension and position of the heterostructure interfaces, the composition of the (Mg,Zn)O alloy (despite correlative microscopy was not the main focus of the article, all this information can be retrieved by the APT analysis itself in a strictly correlative way through the unique features of the PAP), the morphology of the field emitter. The strain model considers both the strain

related to the presence of coherent heterostructure interfaces and the effect of the application of an external bias. It becomes possible to predict the PL energy shifts both as a function of the voltage applied to the emitter, and as a function of the evolution of its shape during the APT analysis. The comparison between the calculations and the experimental data made it possible to determine the applied surface field, the corresponding stress, and the strain state within the tip itself. In this work, the QW was exploited as a localized probe capable of optically transducing the variations of the environmental parameters determining its spectral signature.

The application of the PAP is expected to have further implications in materials science and in the study of the physics of laser-matter interaction in field emitters under high field. Stress-dependent (piezo-spectroscopic) optical measurements can for instance be applied to the determination of deformation potentials in materials in which they are not known. The strain coupling of neighboring quantum emitters can also be studied. In perspective, it would be interesting to perform stress-dependent spectroscopy on quantum dots containing functional impurities. The study of irreversible phenomena could also be achieved: stress-induced dislocation motion or diffusion of point defects within strain gradients could also influence the optical properties of localized emitters. Finally, the photonic coupling of the emitting dipoles to their environment (analyzable for instance through the PL intensity or through the evolution of a time-resolved PL signal) is another domain that can be addressed through the application of the photonic atom probe.

APPENDIX

Strain Hamiltonian and material parameters

For the calculation of strain-dependent energy states, we have adopted the formalism of ref. [39], using the model of Langer et al. [33]. The three valence band energies can be determined as the eigenvalues of the following Hamiltonian:

$$H = \begin{bmatrix} \Lambda_1 & \delta_3 & 0 \\ \delta_3 & \Lambda_2 & \sqrt{2}\Delta_3 \\ 0 & \sqrt{2}\Delta_3 & \Lambda_3 \end{bmatrix} \qquad (11)$$

Where the quantities are:

$$\begin{aligned} \Lambda_1 &= \Delta_1 + \Delta_2 + \delta_1 + \delta_2 \\ \Lambda_2 &= \Delta_1 - \Delta_2 + \delta_1 + \delta_2 \\ \Lambda_3 &= \delta_1 \end{aligned} \qquad (12)$$

$$\begin{aligned} \delta_1 &= D_1\varepsilon_{zz} + D_2(\varepsilon_{xx} + \varepsilon_{yy}) - a_c \\ \delta_2 &= D_3\varepsilon_{zz} + D_4(\varepsilon_{xx} + \varepsilon_{yy}) \\ \delta_3 &= D_5(\varepsilon_{xx} - \varepsilon_{yy}) \end{aligned} \qquad (13)$$

In this expression, Δ_1 is the wurtzite crystal field splitting, Δ_2, Δ_3 represent the spin-orbit coupling, and the δ_i relate the strain to the unperturbed valence bend energy via the deformation potentials D_i.

The materials parameters used for the calculations are given in Tab. 2.

Table 2. Material parameters used in the calculations

Parameter	**Symbol**	**ZnO**	**$Mg_{0.27}Zn_{0.63}O$**	**Notes**
Lattice constants	a	3.246 Å	3.256 Å	Ref. a
	c	5.213 Å	5.182 Å	Ref. a
Elastic constants	C_{11}	238 GPa	238 GPa	Ref. a
	C_{12}	106 GPa	106 GPa	Ref. a
	C_{13}	84 GPa	85.1 GPa	Ref. a
	C_{33}	176 GPa	177.5 GPa	Ref. a
	C_{44}	58 GPa	58 GPa	Ref. a
Band Gap	E_g	3.441 eV	3.891 eV	Ref. a
Valence Band	Δ_1	-0.0383 eV	-	Ref. b
Parameters	Δ_2	0.0021 eV	-	Ref. b
	Δ_3	0.0091 eV	-	Ref. b
Deformation Potentials	D_1	-3.9 eV	-	Ref. b
	D_2	-4.13 eV	-	Ref. b
	D_3	-1.15 eV	-	Ref. b
	D_4	1.22 eV	-	Ref. b
	D_5	1.53 eV	-	Ref. b
	a_c	-3.418 eV	-	Ref. b

Ref. a: [40], Ref. b: [38]

ACKNOWLEDGEMENTS - FUNDING: This work was funded by the French National Research Agency (ANR) in the framework of the projects EMC3 Labex AQURATE, EMC3 Labex IDEPOP and ANR-13-JS10-0001-01 TAPOTER, ANR-11-EQPX-0020 GENESIS and co-funded in the framework of RIN IFROST, EMC3 Labex IDEPOP and CPER BRIDGE projects by European Union with European Regional Development Fund (ERDF) and by Region Normandie. The authors from CRHEA also acknowledge funding from the EU Commission through the ZOTERAC project.

REFERENCES

[1] M. J. Hÿtch, E. Snoeck, and R. Kilaas, *Quantitative Measurement of Displacement and Strain Fields from HREM Micrographs*, Ultramicroscopy **74**, 131 (1998).

[2] M. Hÿtch, F. Houdellier, F. Hüe, and E. Snoeck, *Nanoscale Holographic Interferometry for Strain Measurements in Electronic Devices*, Nature **453**, 7198 (2008).

[3] H. Chen, R. M. Feenstra, R. S. Goldman, C. Silfvenius, and G. Landgren, *Strain Variations in InGaAsP/InGaP Superlattices Studied by Scanning Probe Microscopy*, Appl. Phys. Lett. **72**, 1727 (1998).

[4] P. Offermans, P. M. Koenraad, J. H. Wolter, K. Pierz, M. Roy, and P. A. Maksym, *Atomic-Scale Structure and Photoluminescence of InAs Quantum Dots in GaAs and AlAs*, Phys. Rev. B **72**, 165332 (2005).

[5] G. Wedler, C. M. Schneider, A. Trampert, and R. Koch, *Strain Relief of Heteroepitaxial Bcc-Fe(001) Films*, Phys. Rev. Lett. **93**, 236101 (2004).

[6] D. J. Weidner, M. T. Vaughan, L. Wang, H. Long, L. Li, N. A. Dixon, and W. B. Durham, *Precise Stress Measurements with White Synchrotron x Rays*, Rev. Sci. Instrum. **81**, 013903 (2010).

[7] G. Martínez-Criado, J. Segura-Ruiz, B. Alén, J. Eymery, A. Rogalev, R. Tucoulou, and A. Homs, *Exploring Single Semiconductor Nanowires with a Multimodal Hard X-Ray Nanoprobe*, Adv. Mater. **26**, 7873 (2014).

[8] I. Yeo, P.-L. de Assis, A. Gloppe, E. Dupont-Ferrier, P. Verlot, N. S. Malik, E. Dupuy, J. Claudon, J.-M. Gérard, A. Auffèves, G. Nogues, S. Seidelin, J.-P. Poizat, O. Arcizet, and M. Richard, *Strain-Mediated Coupling in a Quantum Dot–Mechanical Oscillator Hybrid System*, Nat. Nanotechnol. **9**, 2 (2014).

[9] L. Rigutti, G. Jacopin, L. Largeau, E. Galopin, A. De Luna Bugallo, F. H. Julien, J.-C. Harmand, F. Glas, and M. Tchernycheva, *Correlation of Optical and Structural Properties of GaN/AlN Core-Shell Nanowires*, Phys. Rev. B **83**, 155320 (2011).

[10] G. Signorello, S. Karg, M. T. Björk, B. Gotsmann, and H. Riel, *Tuning the Light Emission from GaAs Nanowires over 290 MeV with Uniaxial Strain*, Nano Lett. **13**, 917 (2013).

[11] W. Shan, W. Walukiewicz, J. W. Ager, K. M. Yu, Y. Zhang, S. S. Mao, R. Kling, C. Kirchner, and A. Waag, *Pressure-Dependent Photoluminescence Study of ZnO Nanowires*, Appl. Phys. Lett. **86**, 153117 (2005).

[12] N. Chauvin, A. Mavel, G. Patriarche, B. Masenelli, M. Gendry, and D. Machon, *Pressure-Dependent Photoluminescence Study of Wurtzite InP Nanowires*, Nano Lett. **16**, 2926 (2016).

[13] J.-Y. Kim, D. Jang, and J. R. Greer, *Insight into the Deformation Behavior of Niobium Single Crystals under Uniaxial Compression and Tension at the Nanoscale*, Scr. Mater. **61**, 300 (2009).

[14] G. Signorello, M. Schraff, P. Zellekens, U. Drechsler, M. Bürge, H. R. Steinauer, R. Heller, M. Tschudy, and H. Riel, *An Open-Source Platform to Study Uniaxial Stress Effects on Nanoscale Devices*, Rev. Sci. Instrum. **88**, 053906 (2017).

[15] J. Houard, A. Normand, E. Di Russo, C. Bacchi, P. Dalapati, G. Beainy, S. Moldovan, G. Da Costa, F. Delaroche, C. Vaudolon, J. M. Chauveau, M. Hugues, D. Blavette, B. Deconihout, A. Vella, F. Vurpillot, and L. Rigutti, *A Photonic Atom Probe Coupling 3D Atomic Scale Analysis with in Situ Photoluminescence Spectroscopy*, Rev. Sci. Instrum. **91**, 083704 (2020).

[16] E. Di Russo, P. Dalapati, J. Houard, L. Venturi, I. Blum, S. Moldovan, N. Le Biavan, D. Lefebvre, M. Hugues, J. M. Chauveau, D. C. Blavette, B. Deconihout, A. Vella, F. Vurpillot, and L. Rigutti, *Super-Resolution Optical Spectroscopy of Nanoscale Emitters within a Photonic Atom Probe*, Nano Lett. **20**, 8733 (2020).

[17] J.-M. Chauveau, M. Laügt, P. Venneguès, M. Teisseire, B. Lo, C. Deparis, C. Morhain, and B. Vinter, *Non-Polara-Plane ZnMgO1/ZnO Quantum Wells Grown by Molecular Beam Epitaxy*, Semicond. Sci. Technol. **23**, 035005 (2008).

[18] I. Blum, F. Cuvilly, and W. Lefebvre-Ulrikson, *Chapter Four - Atom Probe Sample Preparation*, in *Atom Probe Tomography* (Academic Press, 2016), pp. 97–121.

[19] L. Rigutti, A. Vella, F. Vurpillot, A. Gaillard, N. Sevelin-Radiguet, J. Houard, A. Hideur, G. Martel, G. Jacopin, A. D. Luna Bugallo, and B. Deconihout, *Coupling Atom Probe Tomography and Photoluminescence Spectroscopy: Exploratory Results and Perspectives*, Ultramicroscopy **132**, 75 (2013).
[20] K. Fisher and E. Marquis, *Comparing Plasma-FIB and Ga-FIB Preparation of Atom Probe Tomography Samples*, Microsc. Microanal. **22**, 692 (2016).
[21] S. Du, T. Burgess, B. Gault, Q. Gao, P. Bao, L. Li, X. Cui, W. Kong Yeoh, H. Liu, L. Yao, A. V. Ceguerra, H. Hoe Tan, C. Jagadish, S. P. Ringer, and R. Zheng, *Quantitative Dopant Distributions in GaAs Nanowires Using Atom Probe Tomography*, Ultramicroscopy **132**, 186 (2013).
[22] E. Di Russo, L. Mancini, F. Moyon, S. Moldovan, J. Houard, F. H. Julien, M. Tchernycheva, J. M. Chauveau, M. Hugues, G. Da Costa, I. Blum, W. Lefebvre, D. Blavette, and L. Rigutti, *Three-Dimensional Atomic-Scale Investigation of ZnO-MgxZn1−xO m-Plane Heterostructures*, Appl. Phys. Lett. **111**, 032108 (2017).
[23] D. Blavette, A. Bostel, J. M. Sarrau, B. Deconihout, and A. Menand, *An Atom Probe for Three-Dimensional Tomography*, Nature **363**, 432 (1993).
[24] B. Gault, F. Vurpillot, A. Vella, M. Gilbert, A. Menand, D. Blavette, and B. Deconihout, *Design of a Femtosecond Laser Assisted Tomographic Atom Probe*, Rev. Sci. Instrum. **77**, 043705 (2006).
[25] G. D. Costa, H. Wang, S. Duguay, A. Bostel, D. Blavette, and B. Deconihout, *Advance in Multi-Hit Detection and Quantization in Atom Probe Tomography*, Rev. Sci. Instrum. **83**, 123709 (2012).
[26] L. Rigutti, L. Venturi, J. Houard, A. Normand, E. P. Silaeva, M. Borz, S. A. Malykhin, A. N. Obraztsov, and A. Vella, *Optical Contactless Measurement of Electric Field-Induced Tensile Stress in Diamond Nanoscale Needles*, Nano Lett. **17**, 7401 (2017).
[27] L. Venturi, L. Rigutti, J. Houard, I. Blum, S. Malykhin, A. Obraztsov, and A. Vella, *Strain Sensitivity and Symmetry of 2.65 EV Color Center in Diamond Nanoscale Needles*, Appl. Phys. Lett. **114**, 143104 (2019).
[28] E. Di Russo, F. Moyon, N. Gogneau, L. Largeau, E. Giraud, J.-F. Carlin, N. Grandjean, J. M. Chauveau, M. Hugues, I. Blum, W. Lefebvre, F. Vurpillot, D. Blavette, and L. Rigutti, *Composition Metrology of Ternary Semiconductor Alloys Analyzed by Atom Probe Tomography*, J. Phys. Chem. C **122**, 16704 (2018).
[29] D. R. Kingham, *The Post-Ionization of Field Evaporated Ions: A Theoretical Explanation of Multiple Charge States*, Surf. Sci. **116**, 273 (1982).
[30] L. Mancini, N. Amirifar, D. Shinde, I. Blum, M. Gilbert, A. Vella, F. Vurpillot, W. Lefebvre, R. Lardé, E. Talbot, P. Pareige, X. Portier, A. Ziani, C. Davesnne, C. Durand, J. Eymery, R. Butté, J.-F. Carlin, N. Grandjean, and L. Rigutti, *Composition of Wide Bandgap Semiconductor Materials and Nanostructures Measured by Atom Probe Tomography and Its Dependence on the Surface Electric Field*, J. Phys. Chem. C **118**, 24136 (2014).
[31] F. Vurpillot, *Chapter Seven - Three-Dimensional Reconstruction in Atom Probe Tomography: Basics and Advanced Approaches*, in *Atom Probe Tomography* (Academic Press, 2016), pp. 183–249.
[32] B. Laumer, F. Schuster, M. Stutzmann, A. Bergmaier, G. Dollinger, and M. Eickhoff, *Accurate Determination of Optical Bandgap and Lattice Parameters of Zn1–XMgxO Epitaxial Films (0≤x≤0.3) Grown by Plasma-Assisted Molecular Beam Epitaxy on a-Plane Sapphire*, J. Appl. Phys. **113**, 233512 (2013).
[33] D. W. Langer, R. N. Euwema, K. Era, and T. Koda, *Spin Exchange in Excitons, the Quasicubic Model and Deformation Potentials in II-VI Compounds*, Phys. Rev. B **2**, 4005 (1970).
[34] K. Hestroffer, R. Mata, D. Camacho, C. Leclere, G. Tourbot, Y. M. Niquet, A. Cros, C. Bougerol, H. Renevier, and B. Daudin, *The Structural Properties of GaN/AlN Core–Shell Nanocolumn Heterostructures*, Nanotechnology **21**, 415702 (2010).
[35] F. Glas, *Critical Dimensions for the Plastic Relaxation of Strained Axial Heterostructures in Free-Standing Nanowires*, Phys. Rev. B **74**, 121302 (2006).
[36] S. Raychaudhuri and E. T. Yu, *Critical Dimensions in Coherently Strained Coaxial Nanowire Heterostructures*, J. Appl. Phys. **99**, 114308 (2006).

[37] L. Rigutti, I. Blum, D. Shinde, D. Hernández-Maldonado, W. Lefebvre, J. Houard, F. Vurpillot, A. Vella, M. Tchernycheva, C. Durand, J. Eymery, and B. Deconihout, *Correlation of Microphotoluminescence Spectroscopy, Scanning Transmission Electron Microscopy, and Atom Probe Tomography on a Single Nano-Object Containing an InGaN/GaN Multiquantum Well System*, Nano Lett. **14**, 107 (2014).
[38] J. Wrzesinski and D. Fröhlich, *Two-Photon and Three-Photon Spectroscopy of ZnO under Uniaxial Stress*, Phys. Rev. B **56**, 13087 (1997).
[39] J.-M. Chauveau, M. Teisseire, H. Kim-Chauveau, C. Morhain, C. Deparis, and B. Vinter, *Anisotropic Strain Effects on the Photoluminescence Emission from Heteroepitaxial and Homoepitaxial Nonpolar (Zn,Mg)O/ZnO Quantum Wells*, J. Appl. Phys. **109**, 102420 (2011).
[40] S.-H. Jang and S. F. Chichibu, *Structural, Elastic, and Polarization Parameters and Band Structures of Wurtzite ZnO and MgO*, J. Appl. Phys. **112**, 073503 (2012).
[41] *Nextnano - Software for Semiconductor Nanodevices*, http://www.nextnano.de/.
[42] F. Vurpillot and X. Sauvage, editors , *Front Matter A2 - Lefebvre-Ulrikson, Williams*, in *Atom Probe Tomography* (Academic Press, 2016), p. iii.
[43] E. P. Silaeva, L. Arnoldi, M. L. Karahka, B. Deconihout, A. Menand, H. J. Kreuzer, and A. Vella, *Do Dielectric Nanostructures Turn Metallic in High-Electric Dc Fields?*, Nano Lett. **14**, 6066 (2014).
[44] M. Lange, J. Kupper, C. P. Dietrich, M. Brandt, M. Stölzel, G. Benndorf, M. Lorenz, and M. Grundmann, *Exciton Localization and Phonon Sidebands in Polar ZnO/MgZnO Quantum Wells*, Phys. Rev. B **86**, 045318 (2012).
[45] A. Ashrafi, *Exciton Localization in Inhomogeneously Broadened ZnO/MgxZn1−xO Quantum Wells*, J. Appl. Phys. **107**, 123527 (2010).
[46] H. Zhu, C. X. Shan, B. H. Li, Z. Z. Zhang, J. Y. Zhang, B. Yao, D. Z. Shen, and X. W. Fan, *Enhanced Photoluminescence Caused by Localized Excitons Observed in MgZnO Alloy*, J. Appl. Phys. **105**, 103508 (2009).
[47] N. Rolland, D. J. Larson, B. P. Geiser, S. Duguay, F. Vurpillot, and D. Blavette, *An Analytical Model Accounting for Tip Shape Evolution during Atom Probe Analysis of Heterogeneous Materials*, Ultramicroscopy **159, Part 2**, 195 (2015).
[48] S. Koelling, A. Li, A. Cavalli, S. Assali, D. Car, S. Gazibegovic, E. P. A. M. Bakkers, and P. M. Koenraad, *Atom-by-Atom Analysis of Semiconductor Nanowires with Parts Per Million Sensitivity*, Nano Lett. **17**, 599 (2017).